PHYSICAL REVIEW D **94,** 034504 (2016)

Thermal dilepton rates and electrical conductivity of the QGP from the lattice

Heng-Tong Ding,[1,*] Olaf Kaczmarek,[2,†] and Florian Meyer[2,‡]
[1]*Key Laboratory of Quark & Lepton Physics (MOE) and Institute of Particle Physics, Central China Normal University, Wuhan 430079, China*
[2]*Fakultät für Physik, Universität Bielefeld, 33615 Bielefeld, Germany*

(Received 10 May 2016; published 15 August 2016)

We investigate the temperature dependence of the thermal dilepton rate and the electrical conductivity of the gluon plasma at temperatures of 1.1, 1.3, and $1.5T_c$ in quenched QCD. Making use of nonperturbatively clover-improved Wilson valence quarks allows for a clean extrapolation of the vector meson correlation function to the continuum limit. We found that the vector correlation function divided by T^3 is almost temperature independent in the current temperature window. The spectral functions are obtained by χ^2 fitting of phenomenologically inspired *Ansätze* for the spectral function to the continuum extrapolated correlator data, where the correlations between the data points have been included. Systematic uncertainties arising from varying the *Ansätze* motivated from strong coupling theory as well as perturbation theory are discussed and estimated. We found that the electrical conductivity of the hot medium, related to the slope of the vector spectral function at zero frequency and momentum, is $0.2C_{em} \lesssim \sigma/T \lesssim 0.7C_{em}$ for $T = 1.1T_c$ and $0.2C_{em} \lesssim \sigma/T \lesssim 0.4C_{em}$ for the higher temperatures. The dilepton rates and soft photon rates, resulting from the obtained spectral functions, show no significant temperature dependence, either.

DOI: 10.1103/PhysRevD.94.034504

I. INTRODUCTION

Ongoing heavy ion collision experiments conducted at facilities like RHIC and LHC provide new output about the nature of elementary particles and their interactions. Direct photons and dileptons (e^+e^-, $\mu^+\mu^-$) are especially good probes of the Quark Gluon Plasma (QGP), as they are produced in all stages of its evolution and, since they are objects underlying the electroweak interaction, their coupling to QGP constituents is small [1,2]; once they are produced, they leave the interaction region largely unmodified. The latest experiments performed at PHENIX and STAR provide indications of thermal enhancements of dilepton spectra in the small to medium frequency region [3,4], which indicates that modifications by the surrounding thermal medium take place. On the other hand, the spectral function in the vector channel at finite temperature provides theoretical information on the thermal dilepton rates accessible in these experiments [5,6], which renders it a worthwhile object to study from theory. Especially the small frequency region of the spectral function contains information on important dynamical quantities like the flavor diffusion constant and the electrical conductivity of the plasma [7,8]. Because this regime is also inherently nonperturbative, the use of lattice QCD data is needed. We attempt to determine the vector channel spectral function for light quark flavors from the theory of QCD. With this we extend our former investigations [9–12]. For other lattice QCD studies, based on finite lattices, see [13–16]. Other determinations of the electrical conductivity can be found in [17–19].

A well-accessible quantity on the lattice is the correlation function in a given mesonic channel. It inhibits dynamical properties of the QGP when investigated at finite temperature. As such, the light vector correlator is related to the electrical conductivity σ of the QGP, the dilepton rate $\frac{\mathrm{d}W}{\mathrm{d}\omega \mathrm{d}^3p}$ and the photon rate $\frac{\mathrm{d}R}{\mathrm{d}^3p}$ as accessible in heavy ion collision experiments, via the vector channel spectral function ρ_V [20,21]. While in general spectral functions relate to correlators through an integral equation,

$$G(\tau, \vec{p}) = \int_0^\infty \frac{\mathrm{d}\omega}{2\pi} \rho_H(\omega, \vec{p}, T) K(\omega, \tau, T) \tag{1}$$

$$\text{with} \quad K(\omega, \tau, T) = \frac{\cosh(\omega(\tau - \frac{1}{2T}))}{\sinh(\frac{\omega}{2T})}, \tag{2}$$

transport coefficients are related to the spectral functions via Kubo formulas. Examples of these are the shear and bulk viscosity obtained from energy momentum tensor correlation functions, the heavy quark momentum diffusion coefficient from color electric correlators [22,23], and the electrical conductivity, related to the light vector spectral function. In the latter case, the Kubo formula is explicitly written as

---

[*] hengtong.ding@mail.ccnu.edu.cn
[†] okacz@physik.uni-bielefeld.de
[‡] fmeyer@physik.uni-bielefeld.de

$$\frac{\sigma}{T} = \frac{C_{em}}{6} \lim_{\omega\to 0} \frac{\rho_{ii}(\omega, \vec{p} = \vec{0}, T)}{\omega T}, \tag{3}$$

with ρ_{ii} denoting only the spatial components of the vector channel and $C_{em} = e^2 \sum q_f^2$ being the sum of the square of the individual quark charges. The two experimentally observable rates mentioned above, originating from processes at all stages of the collisions, can be written in terms of the spectral function in the vector channel and to leading order (LO) read [20,21]

$$\frac{\mathrm{d}W}{\mathrm{d}\omega \mathrm{d}^3 p} = \frac{C_{em}\alpha_{em}^2 \rho_V(\omega, \vec{p}, T)}{6\pi^3(\omega^2 - \vec{p}^2)(e^{\omega/T} - 1)}, \tag{4}$$

$$\omega \frac{\mathrm{d}R_\gamma}{\mathrm{d}^3 p} = \frac{C_{em}\alpha_{em}\rho^T(\omega = |\vec{p}|, T)}{4\pi^2(e^{\omega/T} - 1)}, \tag{5}$$

where ρ_V is again the vector channel spectral function and ρ^T is the spectral function transversally polarized with respect to the direction of $\vec{p}$. These relations imply that once the spectral function of the vector channel is extracted from QCD, important insights into nonperturbative phenomena of heavy ion collisions and the QGP can be gained.

In order to determine the spectral function, however, the Fredholm type-I equation (1) has to be inverted, which is often referred to as an "ill-posed" problem [7]. In our case it is a discrete problem, as we can access the value of the correlation function only at a finite number of points in τT. The basic fact is that the numerical (temporal) correlator data contain $\mathcal{O}(10)$ points, while a solution should be much more fine grained, ideally even continuous. This means that there is more information desired on the rhs than is actually provided on the lhs of Eq. (1). This simple lack of information identifies problem (1) to be principally *underdetermined*. Moreover, the available correlator data points are not known exactly either, as they stem from a Monte Carlo simulation and are subject to statistical uncertainties. This adds to the problem of having only a finite amount of input data. It can be investigated in some cases where it is possible to make a quantitative statement about the connection of fluctuations in the input data and fluctuations in the resulting solution, revealing a strong dependence of the solution on the accuracy of the input data. This has been done in [24], specifically for the Laplace kernel, or [25], where essentially arbitrary integration kernels are considered specifically within the framework of Tikhonov regularization. In addition to the finiteness of the data and their statistical uncertainties, within the framework of lattice QCD an important source of systematic errors is cutoff effects, arising from the lattice regularization itself, that have to be removed by an extrapolation to the physical continuum.

Any approach to solving an ill-posed problem, i.e., regain uniqueness and stability, must add information in order to regularize the problem and thus render it at least "better posed," with two important methods being the already mentioned Tikhonov regularization and the maximum entropy method (MEM) [26,27] or related Bayesian methods [28]. Stochastic approaches for the reconstruction of spectral functions are currently under investigation [29,30]. In a recent study [15] the Backus-Gilbert method was applied for the determination of vector spectral functions and the electrical conductivity.

In the present work we choose the necessary additional information to enter the procedure in the form of a phenomenologically inspired *Ansatz*, which is fitted to continuum extrapolated lattice QCD correlation functions. Fixing the shape of the solution by supplying an *Ansatz* with two or three degrees of freedom is a very strong assumption, and the method of least squares fitting consequently is the natural tool to be employed. Because in this sense the problem has turned into an *overdetermined* one, the choice of the *Ansatz* plays an essential role, and is assessed critically by using different functional shapes in the fit.

The paper is organized as follows. After discussing the setup of the lattice calculation function and the continuum extrapolation of the vector correlation function in the next section, we introduce our *Ansatz* for the spectral function in Sec. III, discuss its properties and the thermal moments derived from it, and analyze the statistical uncertainties of the continuum extrapolated correlators with a special emphasis on the importance of covariances included in our study. Based on this, in Sec. IV we use a class of spectral functions fitted to the continuum correlators to elaborate the systematic uncertainties for the extraction of the vector spectral function. In Sec. V we present our final results for the electrical conductivity, dilepton rates, as well as soft photon rates for the three temperatures used in this work, and conclude in Sec. VI.

II. LATTICE SETUP AND CONTINUUM EXTRAPOLATION

The thermal expectation value of the renormalized Euclidean isovector correlation function,

$$G_H(\tau, \vec{x}) = \langle J_h(\tau, \vec{x}) J_h^\dagger(0, \vec{0})\rangle, \tag{6}$$

is constructed from the renormalized vector current

$$J_h = Z_V \overline{\psi}(x)\gamma_h\psi(x), \tag{7}$$

where Z_V is the appropriate renormalization constant, nonperturbatively determined in [31], and $H = hh = 00$, ii, $\mu\mu$ are components of the vector correlation function. Note that when computing the correlator on the lattice, we do not include the sum of squared charges $C_{em} = \sum_f Q_f^2$, and thus the spectral function obtained from lattice data does not contain this factor, either.

TABLE I. Parameters of all lattices used in this study. The t_0 scale [37], r_0 scale [38], and conversion to T_c are based on [36]. Note that for the continuum extrapolated data we state temperatures of $T = 1.1T_c$, $T = 1.3T_c$, and $T = 1.5T_c$ for the three data sets, respectively.

N_τ	N_σ	β	κ	$T\sqrt{t_0}$	$T/T_c\vert_{t_0}$	Tr_0	$T/T_c\vert_{r_0}$	Configurations
32	96	7.192	0.13440	0.2796	1.12	0.8164	1.09	314
48	144	7.544	0.13383	0.2843	1.14	0.8169	1.10	358
64	192	7.793	0.13345	0.2862	1.15	0.8127	1.09	242
28	96	7.192	0.13440	0.3195	1.28	0.9330	1.25	232
42	144	7.544	0.13383	0.3249	1.31	0.9336	1.25	417
56	192	7.793	0.13345	0.3271	1.31	0.9288	1.25	273
24	128	7.192	0.13440	0.3728	1.50	1.0886	1.46	340
32	128	7.457	0.13390	0.3846	1.55	1.1093	1.49	255
48	128	7.793	0.13340	0.3817	1.53	1.0836	1.45	456

The point to point correlators (6) are projected to definite momentum $\vec{p}$ by summing over all spatial coordinates,

$$G_H(\tau,\vec{p}) = \sum_{\vec{x}} G_H(\tau,\vec{x}) e^{i\vec{p}\,\vec{x}}. \tag{8}$$

In this study we constrain ourselves to the case $\vec{p} = 0$. Results for nonvanishing momenta and how these allow us to obtain lattice constraints on the thermal photon rate can be found in [32].

Splitting the correlation function (8) into spatially and temporally polarized components, defining for $H = V$ in the Euclidean metric $G_V = G_{ii} + G_{00}$, we form a ratio of correlation functions,

$$R_{ii} = \frac{T^2}{\chi_q}\frac{G_{ii}(\tau T)}{G_V^{\text{free,lat}}(\tau T)}, \tag{9}$$

where G_{ii} is normalized by both the free, massless correlator on the lattice [33,34], and the quark number

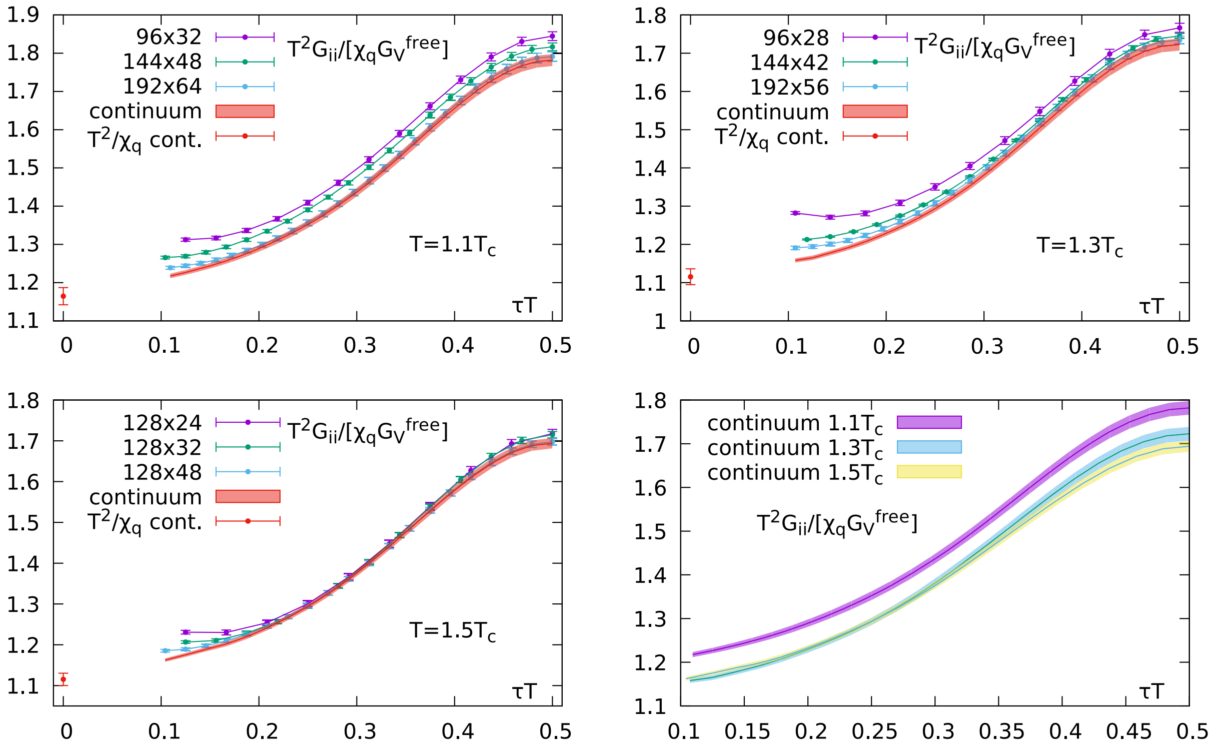

FIG. 1. Left and top right: All three lattice correlators and the resulting continuum extrapolated correlator for the data sets at $T = 1.1T_c$, $T = 1.3T_c$, and $T = 1.5T_c$, respectively. Note that the finest lattice agrees with the continuum extrapolation down to $\tau T \sim 0.2$ in all cases. The single black data point at $\tau T = 0$ indicates the continuum extrapolated result for the inverted quark number susceptibility. Bottom right: The continuum extrapolations for all three temperatures.

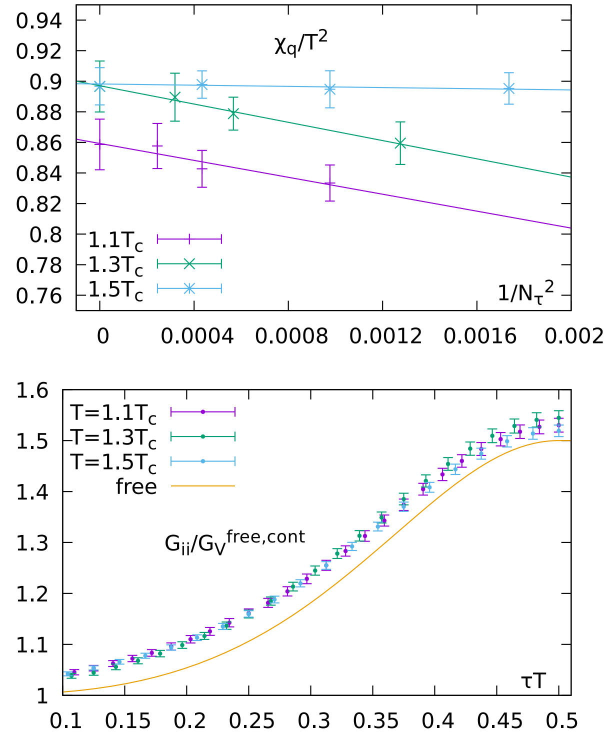

FIG. 2. Top: The extrapolation of χ_q/T^2. The leftmost data points are the continuum extrapolated values. Bottom: Continuum extrapolated ratios of renormalized correlation functions G_{ii}/G_V^{free} for all three temperatures, not normalized by χ_q/T^2. The solid line is the corresponding noninteracting ratio $G_{ii}^{\text{free}}/G_V^{\text{free}}$.

TABLE II. The continuum extrapolated values of the quark number susceptibility χ_q/T^2.

T	$1.1T_c$	$1.3T_c$	$1.5T_c$
χ_q/T^2	0.857(16)	0.897(17)	0.897(12)

susceptibility $\chi_q/T^2 = -G_{00}/T^3$ is defined by the time-time component of the correlation function, which is constant in Euclidean time. The division by the latter is used make the ratio independent of renormalization, while the division by the former cancels the exponential falloff of the interacting correlator.

Lattice calculations have been performed in the quenched approximation using the standard Wilson gauge action with configurations separated by 500 sweeps of over-relaxed heat bath updates, and the nonperturbatively improved Wilson-clover action [35] for the valence quarks. The bare gauge couplings $g^2(a) = 6/\beta$ are fixed to yield three different temperatures $T = 1/(aN_\tau) = 1.1$, 1.3, and $1.5T_c$, with lattice spacings a and lattice time extents N_τ, following the procedure of scale setting recently performed in Ref. [36]. The temperatures and scales quoted in Table I are estimated from the t_0 scale [37] and r_0 scale [38] determined in [36], where also the conversions to T_c for the two different scales are based. For the continuum extrapolated data, in the following, we state temperatures of $T = 1.1T_c$, $T = 1.3T_c$, and $T = 1.5T_c$ for the three data sets, respectively. For each temperature three increasingly finer lattices are considered to allow for linear extrapolations to the continuum limit; see Table I. Valence quark masses are estimated via the improved axial Ward identity mass [35]. The hopping parameters κ are tuned such that the valence quark masses are small, corresponding to $m_{\overline{\text{MS}}}(\mu = 2\ \text{GeV}) \sim \mathcal{O}(10\ \text{MeV})$ in the $\overline{\text{MS}}$ scheme. Note that for the two lowest temperatures the aspect ratio is fixed to $N_\sigma/N_\tau = 3$ and $N_\sigma/N_\tau = 3.42$ for all lattices, respectively, ensuring a constant physical volume, while for the $T = 1.5T_c$ lattices the aspect ratio decreases with decreasing cutoff a. However, finite volume effects are supposed to be small [9].

For each of the three temperatures, all three increasingly fine lattices are used to perform continuum extrapolations of the ratio (9) and the quark number susceptibility χ_q/T^2. In our case, these are linear extrapolations in $1/N_\tau^2 \sim a^2 \to 0$, as opposed to $1/N_\tau \sim a$ for an unimproved Wilson action. In order to carry over a maximum of information from the lattices to the continuum, we interpolate R_{ii} in τT on the two coarser lattices using a natural cubic spline, so that at any distance τT available on the finest lattice the continuum limit can be performed. The results for the ratio (9) are shown in Fig. 1. The errors on the continuum extrapolated ratios are obtained from a bootstrap analysis, and are slightly below the 1% level. For the renormalized quark number susceptibility χ_q/T^2 we show the extrapolation in Fig. 2 (top) and the resulting continuum extrapolated values in Table II. The inverse of the continuum extrapolated susceptibility is also shown in Fig. 1 (left and top right) as red data points in the bottom left corners.

A comparison of the continuum extrapolated ratios for all three temperatures is shown in Fig. 1 (bottom right). The results for the two highest temperatures overlap to a large extent within errors, while the extrapolation for $T = 1.1T_c$ lies above the former. On the other hand, looking at the continuum extrapolated correlator ratio G_{ii}/G_V^{free}, i.e., *without* the dividing by χ_q, for all three temperatures in Fig. 2 (bottom), they show a very pronounced overlap. In the plot the free continuum correlator $G_{ii}^{\text{free}}/G_V^{\text{free}}$ is shown as a solid line and is independent of T. The reason for $R_{ii}(1.1T_c)$ deviating from the almost overlapping $R_{ii}(1.3T_c)$ and $R_{ii}(1.5T_c)$ is thus the quark number susceptibility χ_q/T^2 differing in the two cases, as can be seen from their inverses in Fig 1. However, note that this difference is rather small. From this and the agreement of the correlators in Fig. 2 (bottom), the only scale in this temperature window is the temperature and no resonance contributions, e.g., a rho meson, are expected in the gluon plasma in this temperature region. Additionally it can already be inferred here that the underlying spectral functions should be very similar for all three temperatures, already indicating that temperature effects in the temperature scaled dilepton rates and the electrical conductivities will be rather small.

III. SPECTRAL FUNCTIONS AND THERMAL MOMENTS

In order to extract the vector spectral function via (1) we employ an *Ansatz* for its spatial component, already used before in [9],

$$\begin{aligned}\rho_{\mathrm{ans}}(\omega,T) &= \chi_q c_{\mathrm{BW}} \frac{\omega\Gamma}{\omega^2+(\Gamma/2)^2} \\ &\quad + \frac{3}{2\pi}(1+k)\omega^2 \tanh\left(\frac{\omega}{4T}\right) \\ &\equiv \rho_{\mathrm{BW}}(\omega,T) + (1+k)\rho_V^{\mathrm{free}}(\omega,T). \end{aligned} \tag{10}$$

It consists of two constituents: a Breit-Wigner peak, governing the behavior in the low ω region, and a modified version of the free, massless continuum spectral function. The modification parameter in the latter case fulfils $k = \alpha_s/\pi$ at leading order perturbation theory. As was discussed at the end of the previous section there is no indication of resonances at the temperatures studied in this work and therefore we do not include any bound state contribution in our *Ansatz*. The *Ansatz* (10) is inspired by the known relations for massless continuum spectral functions in the noninteracting case [39],

$$\rho_{ii}^{\mathrm{free}}(\omega,T) = 2\pi T^2 \omega\delta(\omega) + \frac{3}{2\pi}\omega^2 \tanh\left(\frac{\omega}{4T}\right), \tag{11}$$

$$\rho_{00}^{\mathrm{free}}(\omega,T) = 2\pi T^2 \omega\delta(\omega), \tag{12}$$

$$\rho_V^{\mathrm{free}}(\omega,T) = \rho_{ii}^{\mathrm{free}}(\omega,T) - \rho_{00}^{\mathrm{free}}(\omega,T). \tag{13}$$

While the temporal correlator G_{00} also in the interacting case is a constant due to charge conservation, which protects the δ-function contained in its spectral function by symmetry, the corresponding δ-function in the spatial part is expected to be washed out upon the onset of interactions [8,21,40,41] reflecting the transport properties of the thermal medium [42,43]. Following the analysis in [9], motivated by arguments from hydrodynamics and kinetic theory, the δ-function is smeared to a Breit-Wigner peak ρ_{BW} due to thermal modifications. The inverse width of the peak is a measure of the correlation time scale of the medium [7]. In a quasiparticle picture, a larger correlation time implies that there are fewer (or less strong) interactions to wash out existing correlations, and hence the medium is more weakly coupled. Concerning the shape of the resulting spectral function at low frequencies, this is in turn signaled by a narrower peak.

An estimator for the spectral function is then obtained from relation (1) by χ^2-minimizing the *Ansatz* ρ_{ans} from (10) with respect to the continuum extrapolated ratio data from Eq. (9), i.e.,

$$\begin{aligned} R_{ii}(\tau T) &= \frac{T^2}{\chi_q G_V^{\mathrm{free}}(\tau T)} \int_0^\infty \frac{\mathrm{d}\omega}{2\pi} \rho_{ii}(\omega,T) K(\omega,\tau,T) \\ &= \frac{T^3}{2\pi G_V^{\mathrm{free}}(\tau T)} \\ &\quad \times \int_0^\infty \mathrm{d}\left(\frac{\omega}{T}\right) \frac{c_{\mathrm{BW}} T}{\Gamma} \frac{\omega/T}{(\frac{\omega/T}{\Gamma/T})^2 + \frac{1}{4}} K(\omega/T,\tau T) \\ &\quad + \frac{T^2}{\chi_q}(1+k). \end{aligned} \tag{14}$$

Note that, as we have continuum extrapolated data, the free, massless continuum correlation function $G_V^{\mathrm{free}}(\tau T)$, given by

$$\begin{aligned} \frac{1}{T^3} G_V^{\mathrm{free}}(\tau T) &= \frac{1}{2\pi} \int_0^\infty \mathrm{d}\left(\frac{\omega}{T}\right) \rho_V^{\mathrm{free}}(\omega/T) K(\omega,\tau T) \\ &= 6\left\{ \pi(1-2\tau T) \frac{1+\cos^2(2\pi\tau T)}{\sin^3(2\pi\tau T)} \right. \\ &\quad \left. + 2\frac{\cos(2\pi\tau T)}{\sin^2(2\pi\tau T)} \right\}, \end{aligned} \tag{15}$$

appears in the rhs after the integration over ω/T is performed. It thus cancels with the normalizing free spectral function and the free part of the *Ansatz* simplifies to a constant in the fit. The fit itself is performed by taking into account all statistical correlations among the data points, with the covariance matrix $\mathbf{M}$ of the extrapolated continuum ratio $\hat{R}_{ii}(\tau T)$ being estimated from N_{bs} available bootstrap samples $R_{ii}^{(n)}(\tau T)$ via the bootstrap estimator

$$\begin{aligned} M_{jk} &= \frac{1}{N_{bs}} \sum_{n=1}^{N_{bs}} (R_{ii}^{(n)}(\tau T_j) - \hat{R}_{ii}(\tau T_j)) \\ &\quad \times (R_{ii}^{(n)}(\tau T_k) - \hat{R}_{ii}(\tau T_k)). \end{aligned} \tag{16}$$

From the entries of the correlation matrix

$$C_{ij} = \frac{M_{ij}}{\sqrt{M_{ii} M_{jj}}} \qquad \text{(no sum)}, \tag{17}$$

visualized in Fig. 3 (top) for the case $T = 1.1 T_c$, it becomes apparent that there are statistical correlations between data points throughout the whole range of $\tau T > 0.1$. Although they fall off with rising distance, they are still larger than 0.5 for all points that will be considered in the fit and hence

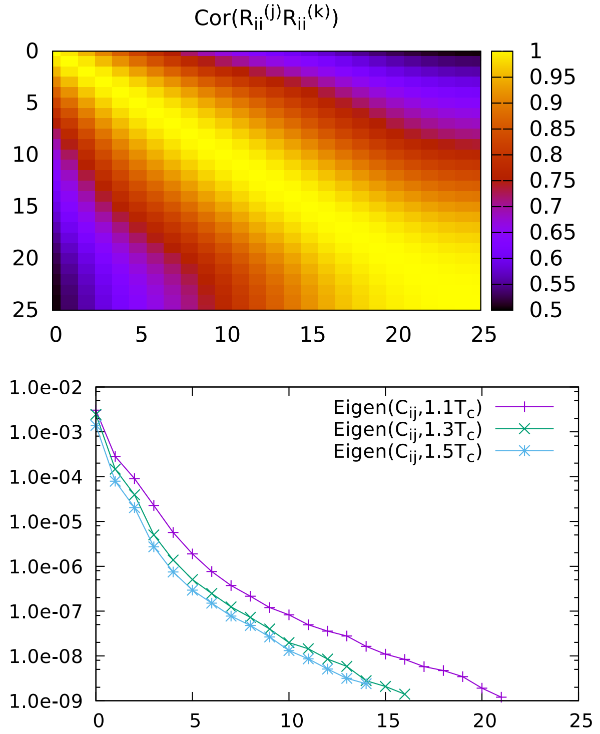

FIG. 3. Top: A heat map of the entries of the estimated continuum correlation matrix for all points $\tau T > 0.1$ at $1.1T_c$. The axes label the row and column entry, respectively. Hence, the midpoint $\tau T_j = \tau T_k = 0.5$ is located in the bottom right corner. Bottom: The eigenvalues of the covariance matrices of the data. Note that they decrease in a regular fashion, without strong fluctuations.

non-negligible in the construction of the χ^2 function. This is in accordance with [9], where the $1.5T_c$ data set has been used for a similar procedure. There the fit is done with only the diagonal parts of the covariance matrix and it yields a very small value of χ^2/dof, which is due to neglecting correlations among the data. Figure 3 (bottom) shows the eigenvalues of the used covariance matrices. Note that the estimated condition number $\sigma_{\max}/\sigma_{\min} \sim 10^6$, with $\sigma_{\min/\max}$ being the smallest/largest eigenvalue of the covariance matrix, is large, but sufficiently small for a stable inversion of C_{ij}.

However, the information about the small ω region resides in the large τT region of the correlator [44], i.e., around its midpoint. In order to extract more information from this region we also extract the second thermal moment of the correlator data and account for it in the fit procedure as an additional data point. The thermal moments are defined by Taylor expanding around the midpoint,

$$G_H(\tau T) = \sum_{n=0}^{\infty} G_H^{(n)} \left(\frac{1}{2} - \tau, T\right)^n, \tag{18}$$

where

$$G_H^{(n)} = \frac{1}{n!} \frac{d^n G_H(\tau T)}{d(\tau T)^n}\bigg|_{\tau T=1/2} \tag{19}$$

$$= \frac{1}{n!} \int_0^{\infty} \frac{\mathrm{d}\omega}{2\pi} \left(\frac{\omega}{T}\right)^n \frac{\rho_H(\omega)}{\sinh(\omega/(2T))}. \tag{20}$$

Because of the symmetry of the integral, the odd thermal moments $G_H^{(2n+1)}$ vanish. The first thermal moment $G_H^{(0)}$ is the value of the correlation function at the midpoint, which is included in the fit trivially, while the second thermal moment $G_H^{(2)}$ is the curvature of the correlation function at the midpoint. In order to extract it from the lattice data, we further define the midpoint subtracted correlator ratio by

$$\Delta_H(\tau T) \equiv \frac{T^2}{\chi_q} \frac{G_H(\tau T) - G_H^{(0)}}{G_H^{\mathrm{free}}(\tau T) - G_H^{(0),\mathrm{free}}}, \tag{21}$$

which at the midpoint satisfies

$$\Delta_H(\tau T) \xrightarrow{\tau T \to 1/2} \frac{T^2}{\chi_q} \frac{G_H^{(2)}}{G_H^{(2),\mathrm{free}}}, \tag{22}$$

hence arriving at a ratio similar to (9). Because we cannot compute the limit (22) directly from the lattice data, we first compute (21) for each lattice spacing for all available distances $\tau T < 0.5$, and extrapolate this to the continuum limit. From (21) and the expansion (18) we find an *Ansatz* to extrapolate the resulting continuum extrapolated midpoint subtracted correlator ratio to $\tau T = 0.5$,

$$\Delta_{ii} = \frac{T^2}{\chi_q} \frac{G_{ii}^{(2)}}{G_{ii}^{(2),\mathrm{free}}} \left\{ 1 + (R_{ii}^{(4,2)} - R_{ii,\mathrm{free}}^{(4,2)}) \left(\frac{1}{2} - \tau T\right)^2 + \mathcal{O}\left(\left(\frac{1}{2} - \tau T\right)^4\right) \right\},$$
$$\text{with } R_X^{(n,m)} = G_X^{(n)}/G_X^{(m)}. \tag{23}$$

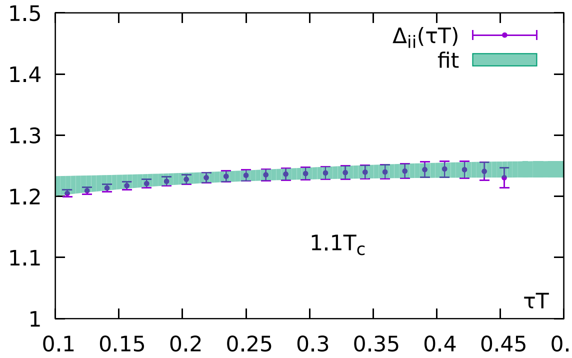

FIG. 4. The necessary extrapolation in τT to obtain Δ_{ii} for the case $T = 1.1T_c$. The fit interval is $\tau T \in [0.2, 0.45]$, i.e., the point at the far right is not included in the fit.

TABLE III. The results for the extrapolation in τT to obtain Δ_{ii}. The fits have been performed using the full covariance matrix of the data.

T	Δ_{ii}	$R_{ii}^{(4,2)}$	χ^2/dof
$1.1T_c$	1.245(14)	10.287(120)	0.67
$1.3T_c$	1.203(12)	10.070(108)	0.50
$1.5T_c$	1.200(9)	10.205(73)	0.89

The two unknown parameters are the thermal moment $G_{ii}^{(2)}/G_{ii,\mathrm{free}}^{(2)}$ and the ratio $R_{ii}^{(4,2)}$. Figure 4 shows the extrapolation for the case $T = 1.1T_c$. The results for Δ_{ii} and the ratio $R_{ii}^{(4,2)}$ are shown in Table III. Note that since the obtained value for the ratio $R_{ii}^{(4,2)}$ is quite accurate, we could also use it to constrain the fits. However, looking at (20), we see that the maximum of the weight $\frac{(\omega/T)^n}{n!\sinh(\omega/(2T))}$ in the integrand is given by the self-consistent expression $\omega/T = 2n\tanh(\omega/(2T))$, which means that for larger n the region of dominating weight shifts to larger frequencies. In turn, this moves the focus further away from the region of interest.

As a remark, it would, in principle, be easier to obtain the second moment from the continuum extrapolated ratio data (9) in a similar fashion by expanding $G_{ii}(\tau T)/G_{ii}^{\mathrm{free}}$ in terms of moments, as we already have it at zero lattice spacing and no additional continuum extrapolation would be necessary. The advantage in constructing the midpoint subtracted correlator ratio from the data from scratch is that the desired second thermal moment then appears in the *Ansatz* (23) as its intercept, while expanding analogously for $G_{ii}(\tau T)/G_{ii}^{\mathrm{free}}$ yields the second thermal moment as its curvature. The former is simply more reliable to obtain from a fit.

IV. ANALYSES OF VECTOR CURRENT CORRELATION FUNCTIONS

When estimating the systematics of our procedure, an essential source of uncertainty is the fit *Ansatz* itself. Because of the general lack of information in an ill-posed inversion problem, and the fact that we add information by choosing our *Ansatz*, which is inspired from phenomenology, it is not excluded that other *Ansätze* fit the data as well. In the next section we thus complement the analysis of *Ansatz* ρ_{ans} by developing several structural changes, and discuss what conclusion could be drawn from the respective modified *Ansatz*. Finally, the fit procedure is applied using each new *Ansatz*, and the results are presented.

A. Spectral function *Ansatz*: Breit-Wigner peak + free continuum

In the fit of our *Ansatz* ρ_{ans} to the extrapolated continuum data we provide as much physical information as possible.

TABLE IV. Results of fitting the *Ansatz* ρ_{ans} for all three temperatures.

T	$\sigma/(C_{\mathrm{em}}T)$	Γ/T	$c_{\mathrm{BW}}T/\Gamma$	k	χ^2/dof
$1.1T_c$	0.302(88)	2.86(1.16)	0.528(154)	0.038(8)	1.15
$1.3T_c$	0.254(51)	3.91(1.25)	0.425(85)	0.029(9)	0.52
$1.5T_c$	0.266(48)	3.33(89)	0.445(80)	0.040(7)	1.13

From the continuum extrapolations shown in Fig. 1 we see that for all three temperatures the extrapolation results almost agree with the data on the corresponding finest lattice from the midpoint down to $\tau T \simeq 0.15$–0.20. This is also where the coarsest lattice starts to bend upwards. As the ratios are supposed to approach $R_{ii} \to T^2/\chi_q$ in the limit $\tau T \to 0$, the "bending up" when going shorter distances is a cutoff effect. Since we want to be sure to include only continuum data, which is free of those effects, into our fit procedure, we aim for $\tau T \sim 0.2$ and in practice take the distance that yields the χ^2/dof closest to unity when fitting *Ansatz* ρ_{ans}. This amounts to $\tau T_{\mathrm{min}} = 0.187$, 0.232, 0.229 for $T = 1.1$, 1.3, $1.5T_c$, respectively, which is also used as a definite choice of fit intervals for all the following fits.

The fits of ρ_{ans} to the continuum extrapolated correlator data show a good convergence behavior and yield as a result the three fit parameters Γ, c_{BW}, and k and their respective statistical fit errors; see Table IV. The relative statistical fit errors of the parameters are roughly 25%–40% for $c_{\mathrm{BW}}T/\Gamma$ and 20%–30% for Γ/T. Note that the former has been calculated taking into account the correlation of the two parameters. The dimensionless modification k to the large frequency free behavior is small, but distinctly larger than 0 in all cases. Their values are reasonable when using the leading order perturbative relation, $k \simeq \alpha_s/\pi$, to compare to other determinations of temperature dependent running couplings [45]. However, within errors there is no visible trend for the available range of temperatures. At this point we treat k or α_s as a constant and do not include a dependence on ω, i.e., a running α_s. In the following subsections we study a class of spectral functions and also model the effect of more involved perturbative large ω behavior in Sec. IV D. The values of χ^2/dof vary around unity and show that the fit to the data performs reliably. Using these parameters and their correlation matrix we construct the resulting spectral function, normalized by the frequency, with its corresponding statistical error band in Fig. 5 (left and top right). The Hard Thermal Loop (HTL) result [46] is also plotted and lies mostly below our estimate of the spectral function. In the low frequency region a straightforward HTL resummation cannot reproduce a finite electrical conductivity as it behaves as $\rho_{\mathrm{HTL}} \sim 1/\omega$ for small ω [46,47].

The electrical conductivity is obtained from the origin of the spectral function via the Kubo relation (3), which is proportional to the ratio of the fit parameters C_{BW} and Γ/T, written as follows:

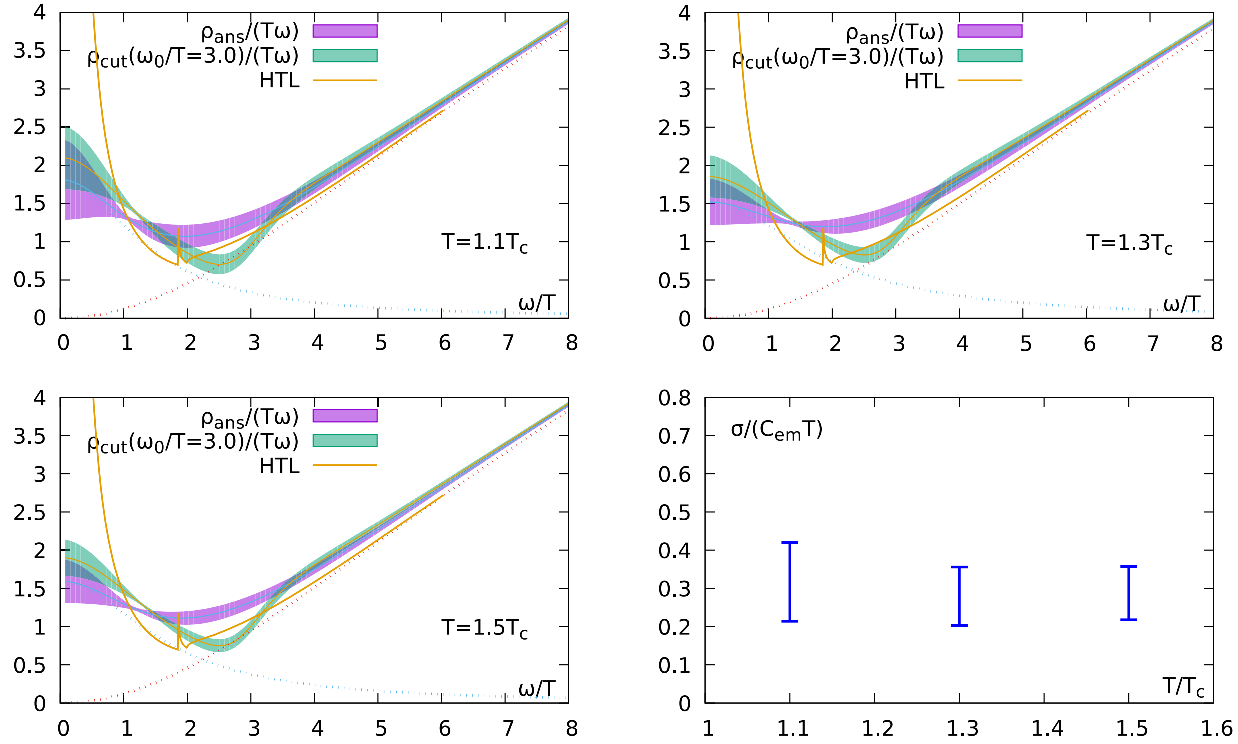

FIG. 5. The spectral functions resulting from the fit for all temperatures. The dotted lines are the Breit-Wigner and the free contributions separately to guide the eye. Note the consistently higher intercept of the spectral functions with the cut applied. Bottom right: The final results for the electrical conductivity for all three temperatures as resulting from *Ansatz* $\rho_{\rm ans}$.

$$\frac{\sigma}{C_{em}T} = \frac{2}{3T}\chi_q \frac{c_{\rm BW}}{\Gamma}. \tag{24}$$

As an intermediate step in our analysis, it is given in Table IV for all three temperatures with the corresponding fitting error. Consequently, the soft photon rate can also be obtained and written in terms of the electrical conductivity as follows,

$$\lim_{\omega\to 0}\omega \frac{\mathrm{d}R_\gamma}{\mathrm{d}^3 p} = \frac{\alpha_{em}C_{em}}{2\pi^2}\left(\frac{\sigma}{C_{em}T}\right)T^2, \tag{25}$$

and is presented at the end of this work, including the systematics developed in the following sections.

B. Spectral function *Ansatz*: flat transport peak + free continuum

The *Ansatz* above is motivated by kinetic theory computations and arguments. On the other hand, in the strong coupling limit the vector spectral function can be obtained from the AdS/CFT correspondence. The resulting spectral function in the low frequency region usually has no peak structure [48], consisting of a flat, "featureless" shape in ρ/ω and then going over into a typical large frequency behavior. This transition is typically accompanied by small, exponentially damped oscillations. A simple *Ansatz* roughly showing this behavior is given by

$$\begin{aligned}\rho_{\rm flat}(\omega) = {}& a\chi_q\omega(1-\tilde{\Theta}(\omega_0,\Delta_0)) \\ & + (1+k)\rho_{\rm free}(\omega)\tilde{\Theta}(\omega_1,\Delta_1),\end{aligned} \tag{26}$$

with ω_i and Δ_i chosen such that ρ/ω then results in the desired shape. The functions $\tilde{\Theta}(\omega_i,\Delta_i)$ are smoothed Heaviside functions

$$\tilde{\Theta}(\omega,\omega_i,\Delta_i) = \left(1+\exp\left(\frac{\omega_i^2-\omega^2}{\omega\Delta_i}\right)\right)^{-1}, \tag{27}$$

which become sharp Heaviside functions in the limit $\Delta_i \to 0$. The cut on the first term is needed to make sure the large frequency regime is not affected by the low frequency constant contribution. This is of course a very rough model: not only is there a certain arbitrariness in the choice of ω_i and Δ_i, but in general there are many possible expressions that approximately describe the desired functional shape. Also, details like the exponentially damped oscillations are not built into this model. For these reasons we do not give definite results for the electrical conductivity or the photon rate, and merely utilize the model to test a nonpeaked, flat low frequency region in ρ/ω. Technically, this change of the *Ansatz*, compared to the previous case, aims at making a statement about the *resolution* of our fit method regarding the low frequency region of the spectral function.

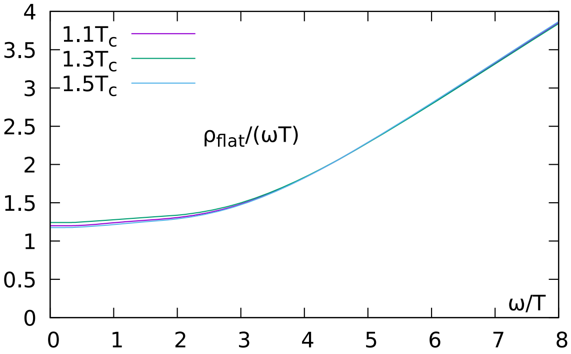

FIG. 6. The spectral function resulting from the fit of the (coarse) model ρ_{flat} for all temperatures.

When fitting ρ_{flat} to the data, we tune the cut positions ω_i and the smoothing parameters Δ_i in such a way that the result from the fit roughly describes the characteristic, featureless ADS/CFT solution. The fits work well for a range of cuts at ω_i and smoothing parameters Δ_i. Throughout all temperatures they yield good fit qualities of $\chi^2/\text{dof} \sim 1.1$ for $T = 1.1{,}1.2T_c$ and $\chi^2/\text{dof} \sim 0.5$ for $T = 1.2T_c$; see Fig. 6 for the resulting spectral functions. The interpretation of this is, first, that qualitatively this type of solution, being featureless in the low frequency region, fits our data just as well as a broad Breit-Wigner peak, motivated by kinetic theory, does. This implies that our method, with regard to the available data, does not have the resolution to differentiate between these two shapes. The second point to make is that when varying the cut positions in such a way that we still have a smooth curve, we always end up with an electrical conductivity that is close to the lower bound of the results presented in Table IV, i.e., when using ρ_{ans}.

C. Cross-check at low frequency

As a rather technical cross-check, instead of using a Breit-Wigner peak for the low frequency part of the spectral function, we change it to be a real δ function with variable height,

$$\rho_\delta(\omega) = a\chi_q\omega\delta(\omega) + (1+k)\rho_V^{\text{free}}(\omega). \tag{28}$$

Up to the parameter k this is essentially the free case. Theoretically, when turning off interactions, the conductivity should approach infinity, since no force changes the state of motion of a charge. Using the Kubo formula, this is clearly reflected in the above *Ansatz* ρ_δ for $\omega \to 0$, i.e., it is incompatible with a finite conductivity. Thus, performing the fit using this *Ansatz* we can check whether this wrong assumption works out with our interacting data, which should definitely yield a *finite* conductivity.

Performing the fit with *Ansatz* ρ_δ we find that the procedure yields values of $\chi^2/\text{dof} \sim 1.5$ for the two lower temperatures, and $\chi^2/\text{dof} \sim 2.5$, for $1.5T_c$, which also quantitatively shows a decrease in fit quality. Looking at the resulting correlators, shown in Fig. 7 (left) for all temperatures, we see that the reconstructed curves really underestimate respectively the correlator data points systematically by an amount of one standard deviation or more. Specifically, the fitted second thermal moments, shown at $\tau T = 0.535$ in the plot, drastically deviate from the data. We conclude that the *Ansatz* does not describe the data sufficiently, and also place an emphasis on the importance of accurately determined thermal moments for the analysis. However, one peculiarity in this case is that, when we perform the fit *without* the covariance matrix in the minimizing χ^2 term, i.e., minimizing only with respect to the diagonal terms, we end up with a function that reconstructs the data points reasonably well at large distances, see Fig. 7 (Right), and also shows the usual small $\chi^2/\text{dof} \sim \mathcal{O}(0.1)$, which is typical for missing correlations. In this case, the second thermal moment is not quite as well reproduced compared to the data points of the ratio $R_{ii}(\tau T)$, but is still distinctly better than in the fully correlated case. Reversing the argument, we see that the *a priori* insufficient

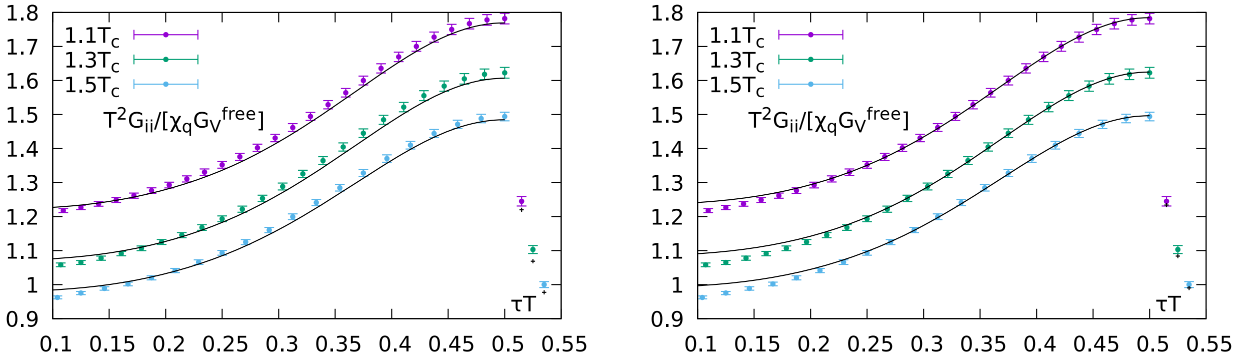

FIG. 7. Fit of a real delta peak in the low frequency region. The points at $\tau T > 0.5$ are the second thermal moments and their fit results, respectively. Left: fit including the covariance of the data. Note how the second thermal moments are described much worse than the corresponding correlator data points. Right: Fit without the covariance of the data. The correlator is described nicely; the thermal moments are a bit off, but less than in the fit including the covariance. The curves are offset for visibility.

fit *Ansatz* ρ_δ, which yields no finite conductivity, fails to describe the data *only* if the information of the full covariance matrix is incorporated in the fit. In this sense we find that including covariances in the fit procedure measurably enhances our resolution of the spectral function in the low frequency region.

D. Uncertainties from the high frequency region

In order to check for uncertainties arising from the way we model the high frequency behavior in ρ_{ans}, we introduce a low frequency cutoff multiplied to ρ_V^{free}, as proposed in [9], so that in total the modified *Ansatz* is given by

$$\rho_{\mathrm{cut}}(\omega, \omega_0, \Delta_0) = \rho_{\mathrm{BW}}(\omega) + (1+k)\rho_V^{\mathrm{free}}(\omega)\tilde{\Theta}(\omega, \omega_0, \Delta_0). \tag{29}$$

The cutoff factor $\tilde{\Theta}(\omega, \omega_0, \Delta_\omega)$ is a representation of the Heaviside function for $\Delta_\omega \to 0$; see Eq. (27). Consider that our choice in ρ_{ans} to account for the large frequency regime is essentially the free vector spectral function. However, this function has positive contributions for all positive frequencies $\omega > 0$, and it influences the Breit-Wigner peak for small frequencies. Thus we probe for this influence by cutting off the low frequency part and observing how the fit results react on this.

In order to fit the function ρ_{cut} to the continuum extrapolated data, we first of all set the width of the smeared Heaviside function to $\Delta_0/T = 0.5$. We varied the value of Δ_0/T and found that the result does not strongly depend on it. Applying the cut to different frequencies ω_0/T has a direct effect on the resulting electrical conductivity, illustrated in Fig. 8. As can be seen, it rises slightly when moving the cut to higher frequencies, showing that the peak rises in height. Around $\omega_0/T \simeq 3$ also Γ/T starts to rise sharply, i.e., at that point the peak is becoming much broader to compensate for the missing free contribution in the low ω regime, and thus $c_{\mathrm{BW}}T/\Gamma$ falls off again. The fit itself still works well over a long range of ω_0 in the sense that χ^2/dof does not change much. However, raising ω_0/T further finally makes the model not fit the data anymore. For the electrical conductivity, we can include its maximal deviation from the result obtained using the untruncated *Ansatz* as an upper systematical error; see Fig. 5 (bottom right). The corresponding spectral function with the cut applied at $\omega_0/T = 3$ is shown in Fig. 5 for all three temperatures.

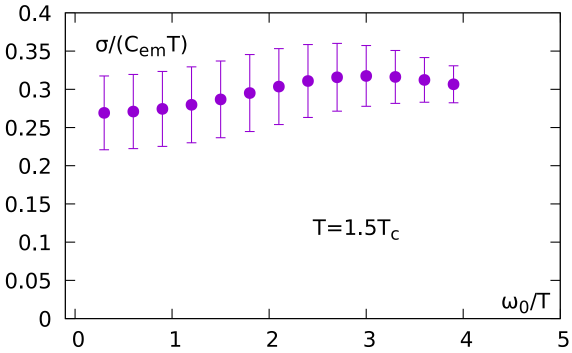

FIG. 8. The increase of electrical conductivity upon the increase of the cutoff ω_0/T in (27). It reaches its maximum around $\omega_0/T \simeq 3$ for all three temperatures. The smoothing parameter is fixed to $\Delta_0/T = 0.5$ throughout the analysis.

In our standard *Ansatz* ρ_{ans} we model the large frequency behavior as a scaled free continuum spectral function. Another approach is to instead incorporate a (higher order) perturbative calculation of the vector channel spectral function. We choose to follow the strategy adopted in [49] and utilize a spectral function that consists of two contributions, first, the LO expression for the vector spectral function in a thermal environment, which just corresponds to $\rho_V^{\mathrm{free}}(\omega)$. Second, we multiply it with the R ratio in the vacuum, computed to N^{4}LO [50,51], altogether leading to

$$\rho_{\mathrm{impr}}(\omega, T) \equiv \rho_V^{\mathrm{free}}(\omega, T)R(\omega^2). \tag{30}$$

In this case we still incorporate a factor multiplying the perturbative spectral function, C, to account for modifications from the surrounding medium, uncertainties in the renormalization, etc. The modified *Ansatz* thus is given by

$$\rho_{\mathrm{R}}(\omega, T) = \rho_{\mathrm{BW}}(\omega, T) + C\rho_{\mathrm{impr}}(\omega, T). \tag{31}$$

Fitting our data with the *Ansatz* ρ_{R} and listing the results in Table V, we generally find that the transport peak becomes a bit narrower and higher, when compared to ρ_{ans}, with the most pronounced effect at $T = 1.1T_c$, where the peak rises one third in height. However, the strong effect at $1.1T_c$ is accompanied by huge errors of both the transport peak's width and height, of 50%–80%. The resulting spectral functions for all three temperatures are shown in Fig. 9. The parameter C is smaller than unity in all cases, and for 1.1 and $1.5T_c$ it is even compatible with unity within its errors. From (31) we see, comparing to the large frequency part of $\rho_{\mathrm{ans}}(\omega)$, that the factor $(1+k)$ corresponds to a factor of $CR(\omega^2)$ in the improved case. On the one hand this makes the improvement of the large frequency part explicit, as the correction coefficient now depends on the frequency. On the other hand, from a purely technical point of view, the remaining *correction constant* C becomes less important for

TABLE V. Results of fitting the *Ansatz* ρ_{R} for all three temperatures.

T	$\sigma/(C_{\mathrm{em}}T)$	Γ/T	$c_{\mathrm{BW}}T/\Gamma$	C	χ^2/dof
$1.1T_c$	0.452(251)	1.62(1.09)	0.790(438)	0.993(7)	1.11
$1.3T_c$	0.301(87)	2.89(1.18)	0.504(145)	0.984(8)	0.53
$1.5T_c$	0.326(87)	2.38(85)	0.548(146)	0.996(7)	1.12

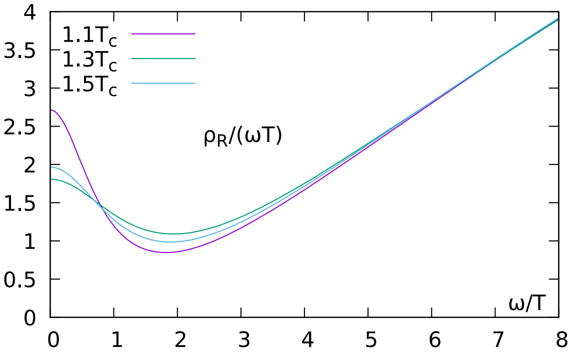

FIG. 9. The resulting spectral function when utilizing perturbative input.

the fit itself, as its deviation from unity is small, and partly negligible within its errors. To state a final result from this *Ansatz*, we plotted the maximum and minimum electrical conductivity, with errors coming from the fit, as the respective right bar of the paired bars in Fig. 5 (bottom right).

V. RESULTS

Comparing the three models ρ_{ans}, ρ_{flat}, and ρ_{R} in Fig. 10 (top left), we see that the area under each peak of the spectral functions is very similar. From a rather sharp peak to a fully flat behavior, all solutions are equally good ones in terms of stability and χ^2. Figure 10 (top right) shows the primitive integral of $\rho/(\omega T)$ for all three cases, which reveals that there is a range of frequencies, roughly $\omega/T \gtrsim 3$, for which the areas under the curves are the same. There is a sum rule found in perturbation theory [21], which states that the area under ρ/ω over the peak region is independent of the coupling, i.e., fixed for our purposes. The authors compute an explicit expression in the framework of kinetic theory, given by

$$\int \mathrm{d}\left(\frac{\omega}{T}\right) \frac{\rho(\frac{\omega}{T})}{\omega T} = \frac{2\pi}{3} N_c, \tag{32}$$

where we suppressed a factor C_{em}, which is not contained in the spectral function we obtain from the continuum extrapolated correlators. We plot this value as a straight line for reference. Information about the exact shape of the spectral function is difficult to obtain using Euclidean data, because for small frequencies $K(\omega, \tau, T) \to 2/\omega$, independent of τ, and thus (1) is fulfilled for any spectral function whose low frequency region has the correct area. This effect we clearly also see in our fit procedure working on nonperturbative continuum data. The sum rule also reflects the small electrical conductivities obtained by fitting ρ_{flat}, compared to the other *Ansätze*, which inhibit peaked structures. As discussed in Sec. III, the width of the peaks, in the *Ansätze* that feature a Breit-Wigner peak at small frequency, is characteristic for the strength of the

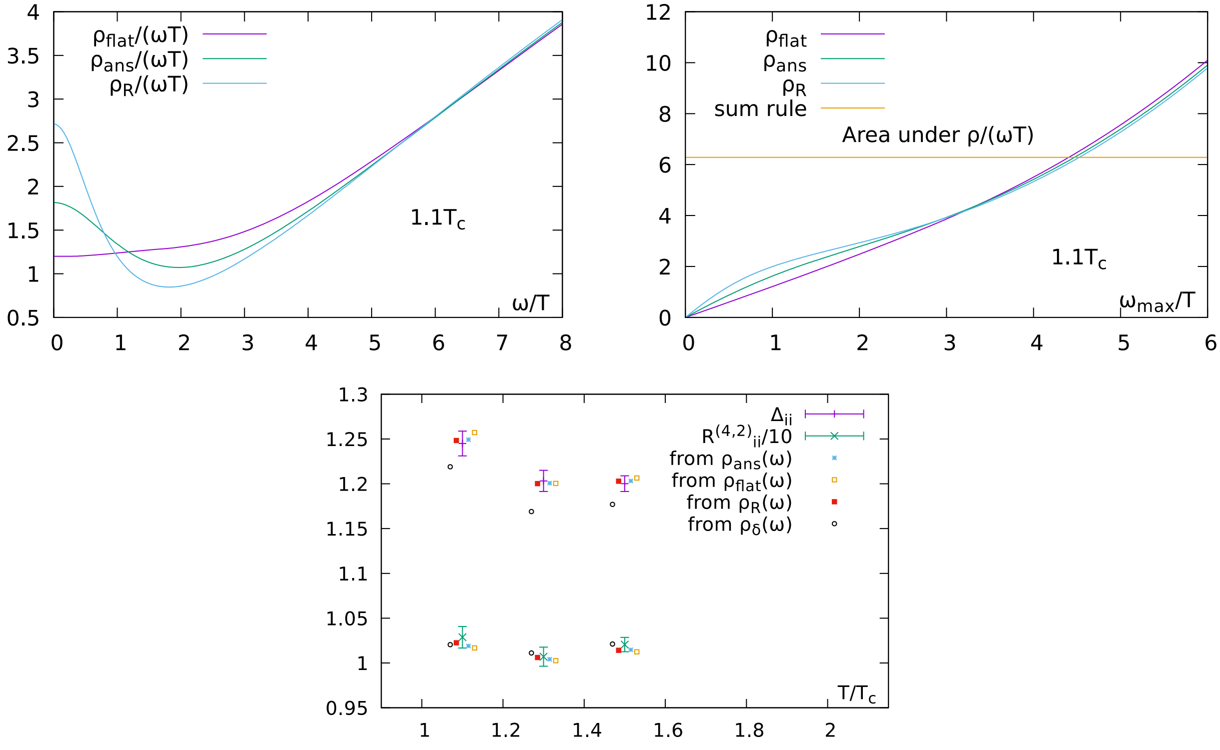

FIG. 10. Top left: The solutions of different *Ansätze* compared for $T = 1.1T_c$. Note that the difference between ρ_{R} and ρ_{ans} is most pronounced at $T = 1.1T_c$. Top right: Integrating $\rho/(\omega T)$ up to ω_{max}, i.e., numerically computing its primitive function for $T = 1.1T_c$. Bottom: The thermal moments for all T and their respective reconstructions from the fit, shown for all three models ρ_{ans}, ρ_{flat}, and ρ_{R}.

interactions in the medium. We generally find $\Gamma/2 \sim \mathcal{O}(T)$ in all of our fits. A width of this order is typical for a strongly coupled regime, and the corresponding scale for a weakly coupled plasma is $\Gamma/2 \sim \mathcal{O}(gT)$ [7], which is parametrically smaller. Thus, our fitting results, obtained using the *Ansätze* motivated from kinetic theory and from the AdS/CFT correspondence, are both in agreement with expectations of a rather strongly coupled medium from 1.1 to $1.5T_c$ and with qualitative features expected from perturbation theory, although perturbative estimates usually overestimate the electrical conductivity for example. Calculations at finite momenta may offer an alternative way to estimate the electrical conductivity as the system becomes more perturbative at the relevant scales as observed in the study in [32], which can be used to further reduce the systematic uncertainties of the spectral function also at zero momentum.

As mentioned before, generally the fits of the models ρ_{ans}, ρ_{part}, and ρ_{flat} to the correlator data yield equally good results, which shows the difficulties in resolving details of the transport region of the spectral function. We find that utilizing the covariance of the data points in the fit generally increases the resolution of the procedure with respect to the low frequency region, as described in Sec. IV C, and also generally enhances the quality of the fit, in the sense that the errors on the resulting parameters are smaller compared to fits without the covariance matrix. The role of the second thermal moment as a constraint in the fit, however, turns out to be a more subtle one: On the one hand, when ignoring the covariance of the data, fitting with the second thermal moment as a constraint essentially also shows the effect of reducing the errors on the resulting fit parameters, as opposed to not constraining the fit with the thermal moment. But this effect does not appear when fitting with the full covariance of the data, showing that the information on the curvature of the correlation function is already largely contained in the statistical correlation. On the other hand, in the fit of $\rho_\delta(\omega)$, done with the full covariance of the data, it still serves as a very strong indication that the fit breaks down. This observation motivates us to also show the reconstruction of the extrapolated second thermal moment and the ratio of the fourth to second thermal moments in Fig. 10 (bottom) for all temperatures. The reconstructed values from the fits [apart from $\rho_\delta(\omega)$] generally are in accord with the second thermal moments as extracted from the data, which underlines that our fits work well from the point of view of fit quality. Although the second thermal moment is especially sensitive to the low frequency region of the spectral function, at the current state of data accuracy we cannot clearly differentiate between the models ρ_{ans}, ρ_{R}, and ρ_{flat} using this observable. Considering that for $T = 1.1T_c$ and $T = 1.5T_c$ the thermal moment for ρ_{flat} deviates from the data visibly, but within errors, increasing the accuracy of the thermal moment data might provide a handle for this. The ratios $R_{ii}^{(4,2)}$ are not included in the fit as a constraint, but *a posteriori* (re) constructed from the data and resulting fit parameters, respectively. They compare within errors, although for $T = 1.1T_c$ and $T = 1.5T_c$ the results from the fit do not compare well. Note that the value from ρ_δ compares as well as any other reconstructed value, unlike in the case of the second moments discussed above. As expected in Sec. III from a rather qualitative argument, we thus see here explicitly that the ratios of the fourth to second thermal moment are indeed far less sensitive to the low frequency region than the second thermal moments.

Our final results for the electrical conductivity for all three temperatures are summarized in Fig. 11 (Right). In the plot we show the respective minimum and maximum value resulting from the two *Ansätze* ρ_{ans} and ρ_{R}, to incorporate the full systematics found in our analysis,

$$\left.\frac{\sigma}{C_{\mathrm{em}}T}\right|_{1.1T_c} = 0.201\text{–}0.703$$

$$\left.\frac{\sigma}{C_{\mathrm{em}}T}\right|_{1.3T_c} = 0.203\text{–}0.388$$

$$\left.\frac{\sigma}{C_{\mathrm{em}}T}\right|_{1.5T_c} = 0.218\text{–}0.413.$$

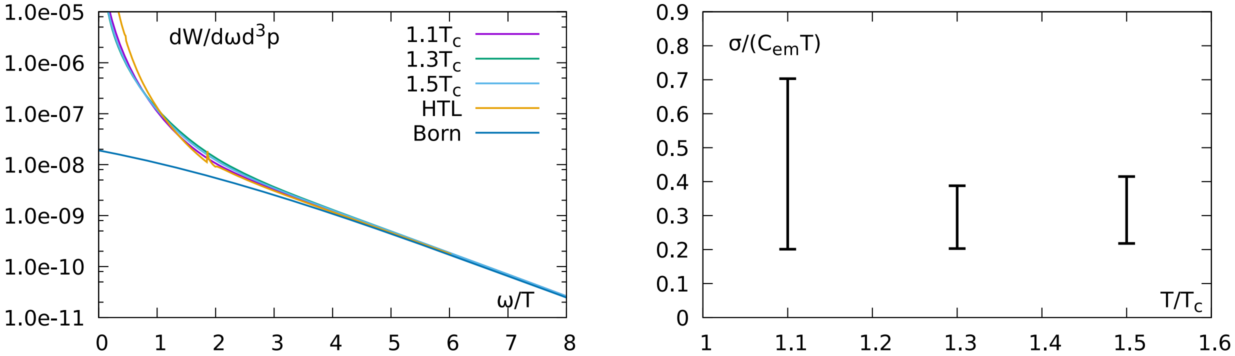

FIG. 11. Left: The thermal dilepton rate as obtained from ρ_{R} as a function of ω/T, accompanied by the HTL rate and the noninteracting Born rate. Right: The final results for the electrical conductivity. They incorporate the full systematics, i.e., the minimum and maximum conductivities, respectively, of ρ_{ans} and ρ_{R}.

In this temperature region they are comparable to recent lattice QCD results using dynamical fermions [15,16,52]. Note that in these studies a drop of the electrical conductivity is observed when going to smaller temperatures around T_c, which may be due to the different nature of the deconfinement transition. For a comparison of recent lattice QCD results see [15] and a comparison of different determinations of the electrical conductivity can be found in [19].

For a comparison of different calculations of the electrical conductivity see [19]. The resulting thermal dilepton rates, obtained from the spectral function ρ_{R} via the first expression of (4), are shown in Fig. 11 (left) for all three temperatures and a sum of squared charges of $C_{em} = \sum_i q_i^2 = 5/9$, corresponding to two valence quark flavors u and d. Our rates are qualitatively comparable to the rate obtained by an HTL calculation [46] in the large frequency region, as well as to the leading order (Born) rate. However, compared to the HTL computation, our results show an enhancement in the intermediate region $\omega/T \sim 2$ and a qualitatively different behavior for small frequency, as the leading term for $\omega \to 0$ is different (see also Fig. 5). Finally, the soft photon rate is given for all temperatures by the electrical conductivity via (25), and $C_{em} = 5/9$, as

$$\omega \frac{\mathrm{d}R_\gamma}{\mathrm{d}p^3}\bigg|_{1.1T_c} = \{5.00\text{–}17.48\} \times 10^{-5} T_c^2,$$

$$\omega \frac{\mathrm{d}R_\gamma}{\mathrm{d}p^3}\bigg|_{1.3T_c} = \{7.05\text{–}13.47\} \times 10^{-5} T_c^2,$$

$$\omega \frac{\mathrm{d}R_\gamma}{\mathrm{d}p^3}\bigg|_{1.5T_c} = \{10.08\text{–}19.18\} \times 10^{-5} T_c^2.$$

The photon rates at the two higher temperatures show a slight trend to rise with temperature, but this is within errors, and for the lower bound alone this trend is true for all T. However, the lowest temperature suffers from a large upper bound, which is also seen in the determined electrical conductivity.

VI. CONCLUSION AND OUTLOOK

Using nonperturbatively improved Wilson-clover valence fermions we performed continuum extrapolations of light vector channel correlation functions at three temperatures. The extrapolations yield reliable results with errors at the subpercent level. A consequence of bootstrapping the extrapolation is that the covariance matrix of the data can be computed and is shown to permit stable fits. Employing a phenomenologically motivated *Ansatz* for the corresponding spectral function, these are used to perform a fully correlated χ^2 minimization and to obtain results for the spectral functions and thus the electrical conductivities via a Kubo relation, the thermal dilepton rates, and the soft photon rates. The second thermal moments, obtained from a separate continuum extrapolation, are found to be sensitive to the low frequency region of the spectral function, while the ratios of the fourth to the second thermal moment are sensitive to a region at larger frequency. Different systematics related to the *Ansatz* are investigated. We find an essential improvement of the fit with respect to the low frequency region when performing the fit fully correlated, as opposed to neglecting the covariances of the data. Fitting a form of *Ansatz* inspired by the phenomenology of a strongly coupled QGP shows a comparable fit quality to the *Ansatz* motivated by a quasiparticle description, which implies that our procedure at this time does not resolve a difference between these two differently shaped spectral functions. This difficulty is reflected by the fact that the different spectral functions, extracted from our nonperturbative data, all fulfil a sum rule that is valid in the low frequency region. However, by observing the resulting peak widths from the fits of a Breit-Wigner peak, we find that they are of the order of $\Gamma/2 \sim \mathcal{O}(T)$, which reveals that both the peaked *Ansätze* and the flat *Ansatz* hint at a strongly coupled medium. The use of a perturbative estimate for the large frequency part of the spectral function is found to generally increase the upper bound of the electrical conductivity. The electrical conductivities are in accordance with earlier results obtained by MEM and χ^2-minimization methods. We find no significant temperature dependence in the temperature range investigated, as was expected from the weak temperature dependence of the correlation functions. The thermal dilepton rates are compared to the HTL and leading order rates and show almost no temperature dependence in the analyzed temperature region, either. The lower bound on the determined soft photon rates clearly follows a trend by rising with temperature. However, the overall large errors, especially at $T = 1.1T_c$, make it difficult to determine a general trend.

The use of a higher order perturbative estimate for the large frequency behavior of our *Ansatz* opens two concrete possibilities. First, because for two temperatures the resulting constant in front of the large frequency part of the spectral function is compatible with unity within errors, we mark that in this sense further improvements might make it superfluous and thus reduce the number of parameters in the fit. Second, the low frequency behavior of the perturbative estimate is merely leading order. By incorporating additional, possibly perturbative, input there, the resolution of the fit in the low frequency region might increase. A fit with a general polynomial *Ansatz* for the low frequency region, and constraints on a smooth connection to the perturbative large frequency behavior, has been done in [32] on the same data as used in this work leading to results in agreement with the ones presented here. Additionally, fits were performed to the same continuum extrapolated vector correlators, but featuring nonvanishing spatial momenta, which allows for an evaluation of photon rates at frequencies $\omega > 0$ and also opens the possibility to estimate the electrical conductivity and diffusion coefficients in general from correlation functions at nonzero momenta. A natural extension of these studies should be an investigation at lower temperatures closer to T_c and below. As light quark degrees of freedom become more important and vector resonance contributions emerge at lower temperatures, this is well justified only in the presence of dynamical quarks.

ACKNOWLEDGMENTS

The results have been achieved using the PRACE Research Infrastructure resource JUGENE based at the Jülich Supercomputing Centre in Germany, the OCuLUS Cluster at the Paderborn Center for Parallel Computing, and the Bielefeld GPU-cluster resources. This work has been partly supported by BMBF under Grants No. 05P12 PBCTA and No. 56268409, NSFC under Grant No. 115 35012, and the GSI BILAER grant. We thank M. Laine, J. Ghiglieri, and the members of the Bielefeld-BNL-CCNU collaboration for fruitful discussions, as well as A. Francis and M. Müller for collaboration at initial stages of this project.

---

[1] G. David, R. Rapp, and Z. Xu, Phys. Rep. **462**, 176 (2008).
[2] Y. Akiba, Prog. Theor. Exp. Phys. **2015**, 03A105 (2015).
[3] A. Adare *et al.* (PHENIX Collaboration), Phys. Rev. C **93**, 014904 (2016).
[4] L. Adamczyk *et al.* (STAR Collaboration), Phys. Rev. C **92**, 024912 (2015).
[5] R. Rapp, J. Wambach, and H. van Hees, in Relativistic Heavy-Ion Physics edited by R. Stock and Landolt-Börnstei, New Series I/23A (Springer, Berlin, 2010), p. 4-1.
[6] D. Bernecker and H. B. Meyer, Eur. Phys. J. A **47**, 148 (2011).
[7] H. B. Meyer, Eur. Phys. J. A **47**, 86 (2011).
[8] J. Hong and D. Teaney, Phys. Rev. C **82**, 044908 (2010).
[9] H.-T. Ding, A. Francis, O. Kaczmarek, F. Karsch, E. Laermann, and W. Soeldner, Phys. Rev. D **83**, 034504 (2011).
[10] A. Francis and O. Kaczmarek, Prog. Part. Nucl. Phys. **67**, 212 (2012).
[11] O. Kaczmarek and M. Müller, *Proc. Sci.* LATTICE2013 (2014) 175 [arXiv:1510.02901].
[12] H.-T. Ding, O. Kaczmarek, and F. Meyer, *Proc. Sci.* LATTICE2014 (2015) 216.
[13] S. Gupta, Phys. Lett. B **597**, 57 (2004).
[14] G. Aarts, C. Allton, J. Foley, S. Hands, and S. Kim, Phys. Rev. Lett. **99**, 022002 (2007).
[15] B. B. Brandt, A. Francis, B. Jäger, and H. B. Meyer, Phys. Rev. D **93**, 054510 (2016).
[16] G. Aarts, C. Allton, A. Amato, P. Giudice, S. Hands, and J.-I. Skullerud, J. High Energy Phys. 02 (2015) 186.
[17] A. Bandyopadhyay, N. Haque, M. G. Mustafa, and M. Strickland, Phys. Rev. D **93**, 065004 (2016).
[18] O. Linnyk, E. L. Bratkovskaya, and W. Cassing, Prog. Part. Nucl. Phys. **87**, 50 (2016).
[19] M. Greif, C. Greiner, and G. S. Denicol, Phys. Rev. D **93**, 096012 (2016).
[20] L. D. McLerran and T. Toimela, Phys. Rev. D **31**, 545 (1985).
[21] G. D. Moore and J.-M. Robert, arXiv:hep-th/0607172.
[22] O. Kaczmarek, Nucl. Phys. **A931**, 633 (2014).
[23] A. Francis, O. Kaczmarek, M. Laine, T. Neuhaus, and H. Ohno, Phys. Rev. D **92**, 116003 (2015).
[24] M. Bertero, P. Boccacci, and E. R. Pike, Proc. R. Soc. A **383**, 15 (1982).
[25] P. Hansen, Numerical Algorithms **46**, 189 (2007).
[26] A. Tarantola, *Inverse Problem Theory and Methods for Model Parameter Estimation* (Society for Industrial and Applied Mathematics, Philadelphia, 2005).
[27] M. Asakawa, T. Hatsuda, and Y. Nakahara, Prog. Part. Nucl. Phys. **46**, 459 (2001).
[28] Y. Burnier and A. Rothkopf, Phys. Rev. Lett. **111**, 182003 (2013).
[29] H.-T. Shu, H.-T. Ding, O. Kaczmarek, S. Mukherjee, and H. Ohno, *Proc. Sci.* LATTICE2015 (2016) 180 [arXiv: 1510.02901].
[30] H. Ohno, *Proc. Sci.* LATTICE2015 (2016) 175.
[31] M. Lüscher, S. Sint, R. Sommer, and H. Wittig, Nucl. Phys. **B491**, 344 (1997).
[32] J. Ghiglieri, O. Kaczmarek, M. Laine, and F. Meyer, arXiv:1604.07544.
[33] S. Stickan, F. Karsch, E. Laermann, and P. Petreczky, Nucl. Phys. B, Proc. Suppl. **129–130**, 599 (2004).
[34] F. Karsch, E. Laermann, P. Petreczky, and S. Stickan, Phys. Rev. D **68**, 014504 (2003).
[35] M. Lüscher, S. Sint, R. Sommer, P. Weisz, and U. Wolff, Nucl. Phys. **B491**, 323 (1997).
[36] A. Francis, O. Kaczmarek, M. Laine, T. Neuhaus, and H. Ohno, Phys. Rev. D **91**, 096002 (2015).
[37] M. Lüscher, J. High Energy Phys. 08 (2010) 071; 03 (2014) 092(E).
[38] R. Sommer, Nucl. Phys. **B411**, 839 (1994).
[39] G. Aarts and J. M. Martinez Resco, Nucl. Phys. **B726**, 93 (2005).
[40] G. Aarts and J. M. Martinez Resco, J. High Energy Phys. 04 (2002) 053.
[41] P. Petreczky and D. Teaney, Phys. Rev. D **73**, 014508 (2006).
[42] J. Boon and S. Yip, *Molecular Hydrodynamics* (McGraw-Hill, New York, 1980).
[43] D. Forster, *Hydrodynamics, Fluctuations, Broken Symmetry, and Correlation Functions*, Frontiers in Physics (Westview Press, 1995).
[44] G. Aarts and J. M. Martinez Resco, Nucl. Phys. B, Proc. Suppl. **119**, 505 (2003).

[45] O. Kaczmarek, F. Karsch, F. Zantow, and P. Petreczky, Phys. Rev. D **70**, 074505 (2004); **72**, 059903 (2005).

[46] E. Braaten and R. D. Pisarski, Nucl. Phys. **B337**, 569 (1990).

[47] F. Karsch, M. G. Mustafa, and M. H. Thoma, Phys. Lett. B **497**, 249 (2001).

[48] D. Teaney, Phys. Rev. D **74**, 045025 (2006).

[49] Y. Burnier and M. Laine, Eur. Phys. J. C **72**, 1902 (2012).

[50] P. A. Baikov, K. G. Chetyrkin, and J. H. Kuhn, Phys. Rev. Lett. **101**, 012002 (2008).

[51] P. A. Baikov, K. G. Chetyrkin, and J. H. Kuhn, Nucl. Phys. B, Proc. Suppl. **189**, 49 (2009).

[52] A. Amato, G. Aarts, C. Allton, P. Giudice, S. Hands, and J.-I. Skullerud, Phys. Rev. Lett. **111**, 172001 (2013).